Supplementary Information for

Experimental Realization of a Reconfigurable Electroacoustic Topological Insulator

Amir Darabi, Manuel Collet, and Michael J. Leamy

Corresponding Author: Michael J. Leamy
E-mail: michael.leamy@me.gatech.edu

This PDF file includes:

Supplementary text
Figs. S1 to S7
References for SI reference citations

www.pnas.org/cgi/doi/10.1073/pnas.1920549117

Supporting Information Text

1. Supplementary Note 1: Dispersion curves

A. Equations of motion and band structures. A first step towards designing a topological insulator is to compute the band structure along the edges of the Brillouin zone in order to realize Dirac cones at the $K-$points (in the case of a hexagonal lattice). Herein, a composite unit cell is made by bonding two 0.5 mm piezoelectric disks (PZT) to a host layer (PLA) of thickness 0.5 mm. The host layer is modeled as a linear isotropic material, rigidly bonded to each PZT disk. The equations of motion for this composite is governed by,

$$\rho\ddot{\mathbf{U}} = \nabla.S \quad [1]$$

$$S = \mathbf{c}(E_0) : \varepsilon(\mathbf{U}) - \mathbf{e}^T\mathbf{E} \quad [2]$$

$$\nabla.\mathbf{D} = \rho_v \quad [3]$$

$$D = \mathbf{e}\varepsilon(\mathbf{U}) + \epsilon_{rs}\mathbf{E}, \quad [4]$$

where $\mathbf{U}(x,y,z) = u\hat{i} + v\hat{j} + w\hat{k}$ denotes the displacement vector, ρ the mechanical density, $\nabla.$ the divergence operator, S the stress matrix, $\mathbf{c}(E_0)$ the fourth order elasticity tensor, E_0 the modulus of elasticity, $\varepsilon(\mathbf{U})$ the strain matrix, $\mathbf{D}$ the electrical charge, ρ_v the electrical charge density, $\mathbf{e}$ the coupling matrix of the piezoelectric, $\mathbf{E}$ the electrical field, and ϵ_{rs} the relative permitivity. Note that for the linear elastic material (i.e., PLA in absence of the PZT), the governing equations are arrived at by setting all electrical terms to zero. Figure S1(a) displays a PLA ($E = 3.5\ GPa$, $\rho = 1300\ kg/m^3$, $\nu = 0.3$) hexagonal honeycomb unit cell bonded to two piezoelectric disks (PZT4) of diameter 7 mm. Each of these unit cells are then repeated periodically in the $\mathbf{a_1} = L\hat{i}$, $\mathbf{a_2} = L/2\hat{i} + \sqrt{3}L/2\hat{j}$ lattice directions to form the phononic crystal. Bloch boundary conditions in COMSOL Multiphysics, with appropriate destinations on the edges, are used to compute the band structure by sweeping the wavenumber along the boundaries of the first irreducible Brillouin zone (blue triangular area in Fig. S1(b)),

$$\Gamma = (0,0) \quad [5]$$

$$M = (0, 2\pi/\sqrt{3}) \quad [6]$$

$$K = (2\pi/3, 2\pi/\sqrt{3}). \quad [7]$$

Figure S1(c) displays the band structure in the absence of any external circuit for the frequency range of interest in this work. As shown, two degenerate Dirac cones are observed at the K-point.

B. System connected to an external circuit. One possible way to vary the piezoelectric stiffness is to employ shunted piezoelectric disks. Figure S2 depicts a piezoelectric disk attached to an external circuit. When a piezoelectric patch is connected to an active circuit with the capacitance of $-C'$, the elastic stiffness can change dramatically (1–5). As shown in Fig. S2**(a)**, the equivalent negative capacitance of the circuit is given by,

$$-C' = -\frac{R_2 C_0}{R_1}, \quad [8]$$

where R_1 and R_2 are the resistors connected to the OP-AMP, and C_0 is the paralleled capacitor. Although the material properties of these disks can change by varying the negative capacitance, they are stable only for $C' > C_p^T$ (6), where C_p^T is the internal capacitance of the PZT at short circuit. In addition, to prevent saturation of the capacitor, which can also lead to instability, a resistor (R_0) with a relatively large resistance compared to R_1 and R_2 is paralleled with the capacitor (7). Finally, as shown in Fig. S2, by placing a switch between the piezoelectric and the circuit, we can connect/disconnect the PZT disk to the external circuit. Figure S2**(b)** plots the band structure for a range of negative capacitance values. As shown, by decreasing the value of negative capacitance, the topological bandgap becomes wider, until this value reaches its optimal value for $C' = -1.7nF$. Further decreasing the value of the negative capacitance results in deforming the bands bounding the topological bandgap, and increasing the chance of destabilizing the piezoelectric disks.

2. Supplementary Note 2: Chern numbers

For any dispersion curve bounding the topological band-gap, the Berry connection is defined as (8),

$$\mathscr{A}(\mathbf{k}) = \langle \mathbf{U}(\mathbf{k}) | i\nabla_{\mathbf{k}} | \mathbf{U}(\mathbf{k}) \rangle, \quad [9]$$

where $\mathbf{U}(\mathbf{k})$ is the mass-normalized displacement of the eigenmode computed at the wave-vector $\mathbf{k}$, $\nabla_{\mathbf{k}} = \frac{\partial}{\partial_{kx}}\hat{i} + \frac{\partial}{\partial_{ky}}\hat{j}$, and $i = \sqrt{-1}$ is the unit imaginary number. The Berry curvature of a given mode is defined as $\mathscr{F} = \nabla_{\mathbf{k}} \times \mathscr{A}$. Figure S3 displays the Berry curvature of the system shown in Fig. 1(a-b) of the main manuscript. Finally, the valley Chern number of each mode is computed as the integral of the Berry curvature over half of the Brillouin zone (9),

$$C_v = \frac{1}{2\pi} \iint \left(\frac{\partial \mathscr{A}_{k_y}}{\partial k_x} - \frac{\partial \mathscr{A}_{k_x}}{\partial k_y} \right) dk_x\, dk_y \quad [10]$$

For the system proposed in this study, the valley Chern numbers are computed to be $\{+1/2, -1/2\}$.

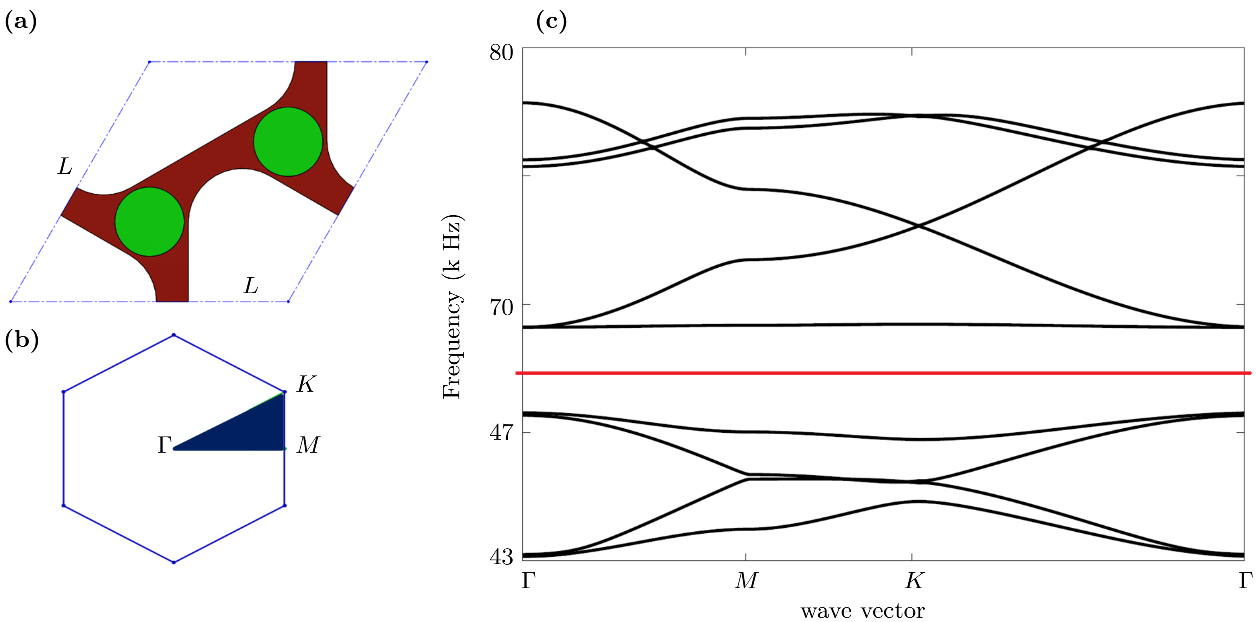

Fig. S1. **(a)** Schematic of the proposed hexagonal unit cell in this work (with the size of L), composed of a PLA host layer with two bonded piezoelectric disks, **(b)** Schematic of the Brillouin zone of the proposed hexagonal unit cell, **(c)** Band structure of the hexagonal unit cell.

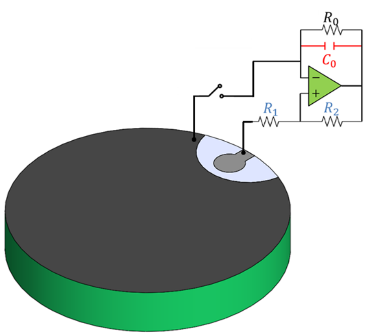

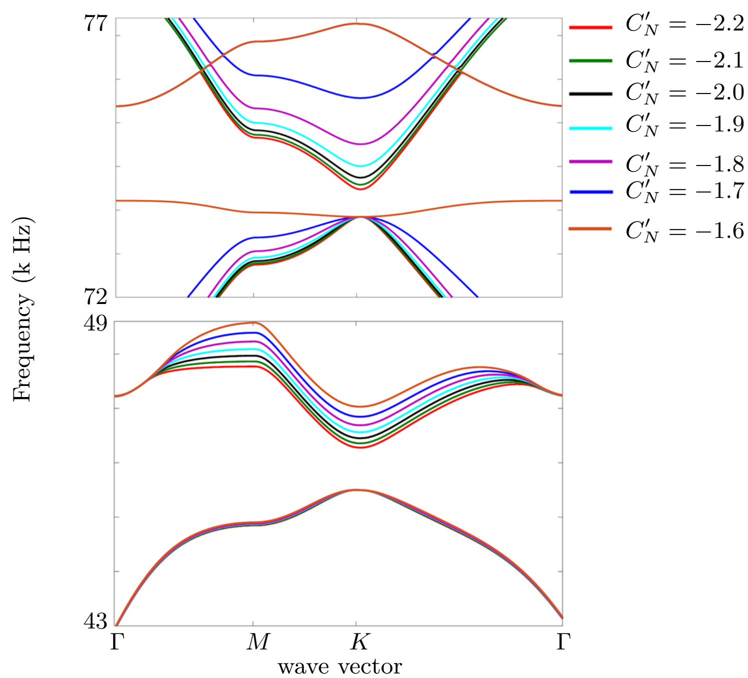

Fig. S2. (a) Schematic of a shunted piezoelectric disk and its connected circuit. **(b)** Band structure of the hexagonal unit cell for different values of negative capacitance plotted for two different ranges of frequency.

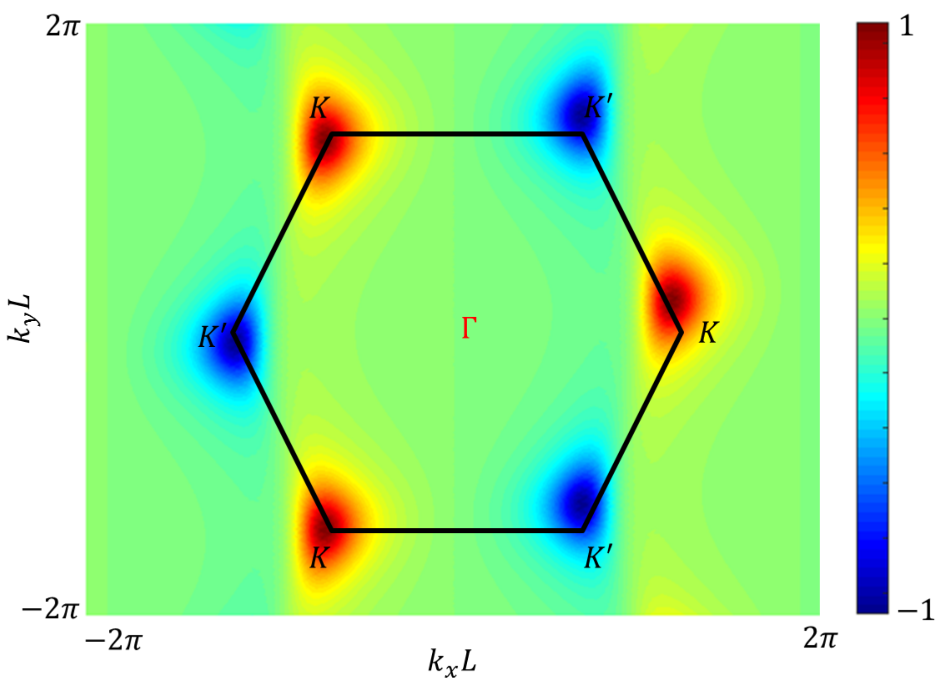

Fig. S3. The Berry curvature of the system proposed in Fig. 1(a-b) of the main manuscript for the topological bandgap with a higher frequency (i.e., the band above the bandgap).

3. Supplementary Note 3: Absence of standing waves

The topology of the studied waves offers protection from back-scattering, and thus the avoidance of standing waves in the considered structure. To verify this property, a small control volume at one of the unit cells is considered (as shown in Fig. S4). Then, the input and output power into the control volume (marked with vertical lines) is computed based on the experimental data. Finally, the input and output control volume energy is determined by integrating each power over five periods. The computed value for the input energy is 2.340 J, while the output is 2.176 J, representing a 7% difference. This difference results from stored energy in the control volume (i.e., standing wave energy) and dissipated energy. Its small value clearly confirms that little standing wave energy is generated by the propagating waves.

4. Supplementary Note 4: Experiment

A. Setup. Figure S5 depicts the fabricated structure (on the left) and the external circuit (on the right). This structure is realized by machining a 0.5 mm thickness PLA plate ($E = 3.5\ GPa$, $\rho = 1300\ kg/m^3$, $\nu = 0.3$) and bonding (using 3M DP270 Epoxy Adhesive) 50 piezoelectric disks (PZT4). Each piezoelectric disk has a 7 mm diameter and a 0.5 mm thickness. For each circuit wired to the PZT disks, negative capacitance $C' = -1.7\ nf$ is obtained by using $R_1 = 10, R_2 = 17\ \Omega$, $C_0 = 1\ nF$, and $R_0 = 1\ M\Omega$. A Polytec PSV-400 scanning laser Doppler vibrometer measures the resulting out-of-plane wavefield velocity using the backside of the PLA plate, repeating and averaging each measurement 10 times (in order to reduce the influence of noise). In order to generate waves into the system, one of the bonded piezoelectric disks is connected to a $150mV$ (peak-to-peak) burst sinusoidal signal, using a function generator (Agilent 33220A) coupled to a voltage amplifier (B&K1040L). Proper triggering of the laser measurements allows reconstruction of the out-of-plane velocity field. Finally, in order to decrease the boundary effects at the location of the source, absorbing patches are used to reduce the leakage of propagation waves on the edge.

B. Time snapshots of experimental results. Figures S6 and S7 plot snapshots of the experimentally measured wavefield for the two interfaces reported in the manuscript at different points in time. The maximum distance that waves can travel in one period are computed from the group velocity of band diagrams in Fig. 2 to be 3 mm. For the horizontal interface depicted in Fig. S5, the time values are $t_1 \approx 4T$, $t_2 \approx 11T$, $t_3 \approx 23T$, and $t_4 \approx 38T$, respectively. On the other hand, for the angled interface shown in Fig. S6, these time values are $t_1 \approx 4T$, $t_2 \approx 12T$, $t_3 \approx 20T$, and $t_4 \approx 34T$, respectively. Based on the calculated maximum distance that waves can travel, the wave should propagate from the source to the receiver in a time equal to approximately 40 times the propagation the period, which is in a good agreement with the time values reported above.

References

1. Hagood NW, von Flotow A (1991) Damping of structural vibrations with piezoelectric materials and passive electrical networks. *Journal of Sound and Vibration* 146(2):243–268.
2. Beck BS, Cunefare KA, Collet M (2013) The power output and efficiency of a negative capacitance shunt for vibration control of a flexural system. *Smart Materials and Structures* 22(6):065009.
3. Beck BS (2012) Ph.D. thesis (Georgia Institute of Technology).
4. Tateo F, et al. (2015) Experimental characterization of a bi-dimensional array of negative capacitance piezo-patches for vibroacoustic control. *Journal of Intelligent Material Systems and Structures* 26(8):952–964.
5. Park J, Palumbo DL (2004) A new approach to identify optimal properties of shunting elements for maximum damping of structural vibration using piezoelectric patches.
6. De Marneffe B, Preumont A (2008) Vibration damping with negative capacitance shunts: theory and experiment. *Smart Materials and Structures* 17(3):035015.
7. Trainiti G, et al. (2019) Time-periodic stiffness modulation in elastic metamaterials for selective wave filtering: Theory and experiment. *Physical review letters* 122(12):124301.
8. Adrian HCP (2011) Ph.D. thesis (The Chinese University of Hong Kong).
9. Ma J, Sun K, Gonella S (2019) Valley-hall in-plane edge states as building blocks for elastodynamic logic circuits. *arXiv preprint arXiv:1904.01647*.

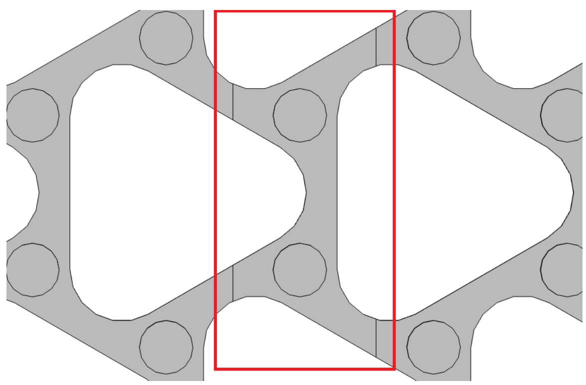

Fig. S4. A schematic of the considered control volume to calculate the amount of standing waves.

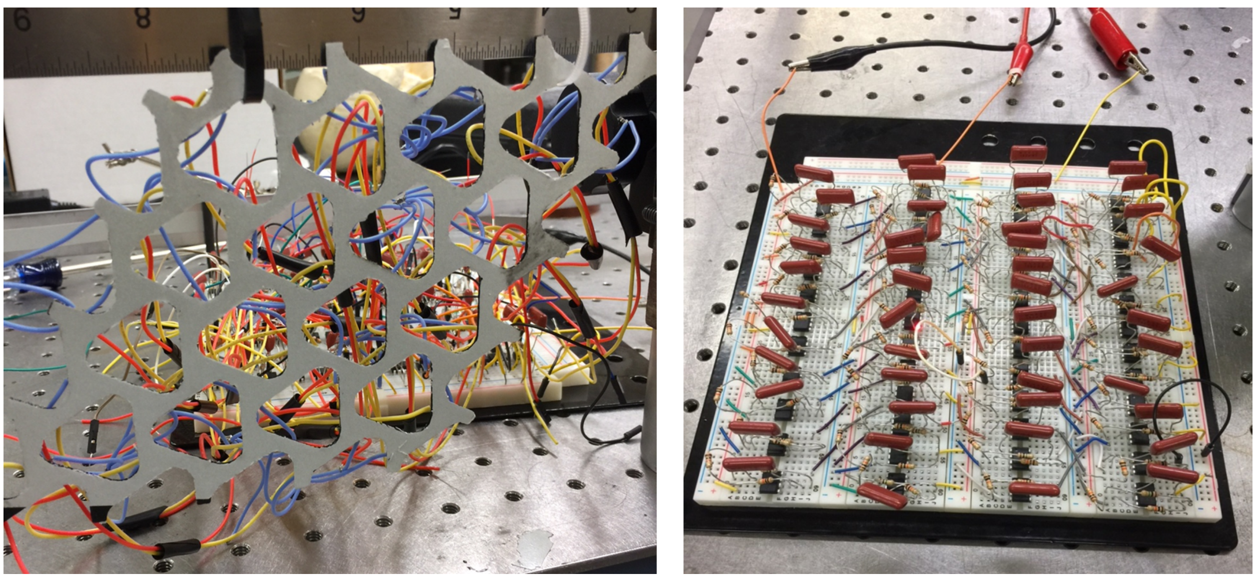

Fig. S5. Fabricated experimental setup. On the left: the tested structure wired to the external circuits. On the right: the external circuits used to provide negative capacitance.

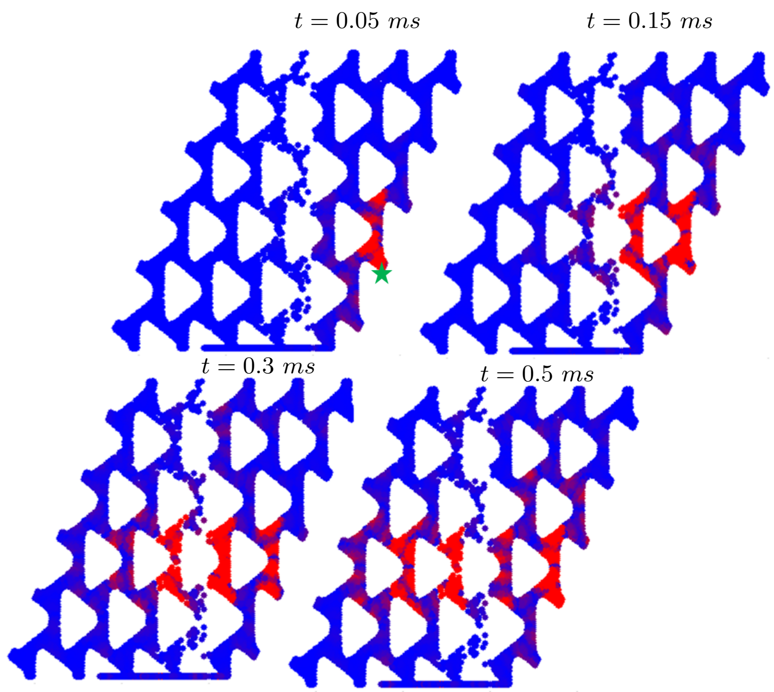

Fig. S6. Experimentally measured displacement field of the system with a horizontal interface (depicted in Fig. 4(b) of the manuscript) captured at different times, excited by a source with frequency $77\ kHz$. The source location is marked with a green star.

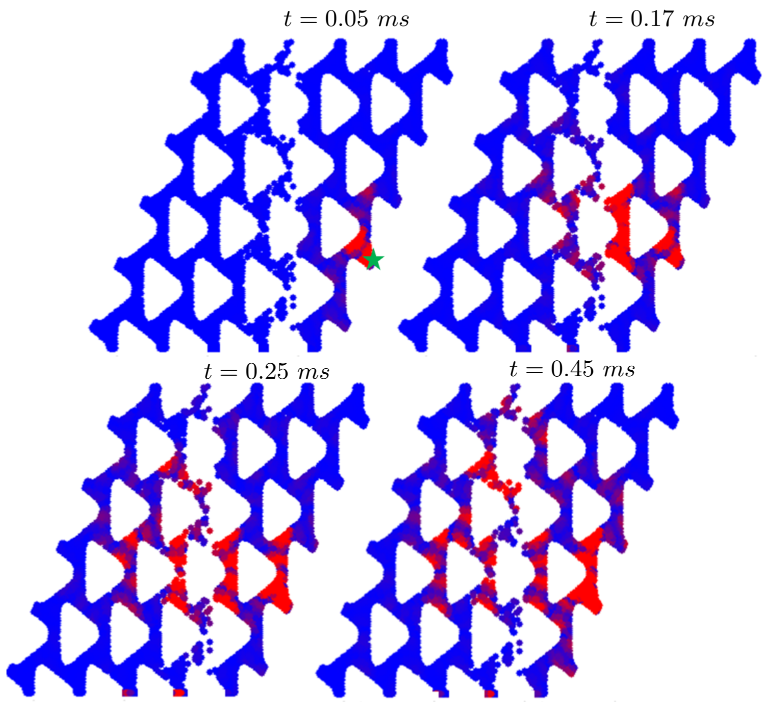

Fig. S7. Experimentally measured displacement field of the system with a sharp-angled interface (depicted in Fig. 4(b) of the manuscript) captured at different times, excited by a source with frequency $77\ kHz$. The source location is marked with a green star.